

Design and Realization of a Highly-Compact Tubular Linear Actuator for a Novel Total Artificial Heart

Rosario V. Giuffrida¹, *Student Member, IEEE*, Raffael Senti¹, Johann W. Kolar¹, *Fellow, IEEE*, Tim Bierewirtz², Krishnaraj Narayanaswamy³, Marcus Granegger^{2,3} and Dominik Bortis¹ *Senior Member, IEEE*

¹Power Electronic Systems Laboratory, ETH Zurich, Zurich, Switzerland

²Institute of Computer-Assisted Cardiovascular Medicine, Charité-Universitätsmedizin Berlin, Corporate Member of Freie Universität Berlin and Humboldt-Universität zu Berlin, Berlin, Germany

³Department of Cardiac Surgery, Medical University of Vienna, Vienna, Austria
giuffrida@lem.ee.ethz.ch

Abstract—The *ShuttlePump* is a novel implantable total artificial heart (TAH) concept based on a Linear-Rotary Actuator (LiRA) and currently under development at the Power Electronic Systems Laboratory, ETH Zurich in close partnership with Charité Berlin and the Medical University of Vienna. This paper presents the analysis, design and realization of the *ShuttlePump* Linear Actuator (LA) part, which is necessary to provide about 45 N of axial actuation force. Design criteria are minimization of volume and generated power losses in the winding, which could result in excess heating and/or blood damage, i.e. protein denaturation and aggregation. The LA is implemented as a Tubular LA (TLA) to maximize the active area for linear/axial force generation. After a preliminary analysis based on first principles, the TLA is optimized in detail with the aid of FEM simulations. The experimental measurements conducted on the realized TLA prototype verify the FEM simulation results and confirm the suitability for the realization of the *ShuttlePump* TAH.

I. INTRODUCTION

Heart failure is a serious disease affecting currently more than 26 million people worldwide and the number of cases is expected to increase in the near future, also due to the progressive aging of the population [1]. Although heart transplantation remains the preferred long-term treatment for end-stage heart failure, the availability of organs from donors is very limited, with up to 20% of patients dying while on the waiting list [2]. For these reasons, there is an urgent need for alternative solutions. Mechanical Circulatory Support (MCS) devices, in the form of Ventricular Assist Devices (VADs) or Total Artificial Hearts (TAHs), have the potential to address this need.

Implantable VADs are already in use as a long-term solution and are e.g. comparable to a post-heart transplantation in terms of survival rates in the first years of implantation [3]. Unfortunately, they do not represent an adequate solution in the case of biventricular failure, where it would be preferable to replace the failing heart completely with a TAH instead. However, differently from VADs, no durable TAH designed for long-term application is currently approved for clinical use [4], [5].

An example of this strive for next-generation TAHs is the *ShuttlePump* (cf. Fig. 1), an implantable TAH currently under development at the Power Electronic Systems Laboratory, ETH Zurich in partnership with Charité Berlin and the Medical University of Vienna [6], [7]. As explained more in detail

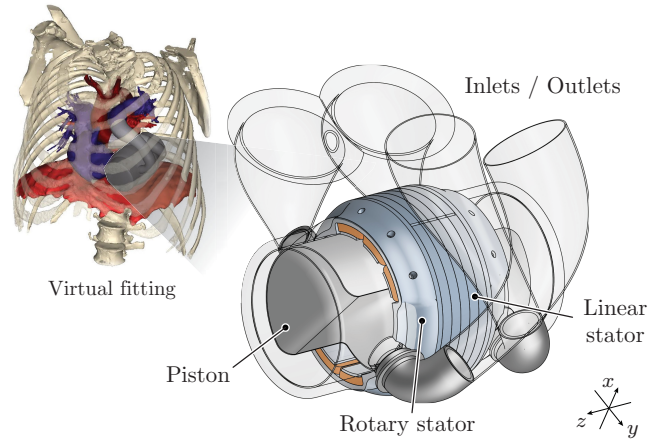


Fig. 1: The implantable TAH *ShuttlePump*, conceptual illustration with virtual fitting in a patient with biventricular failure (ethics approval obtained at Medical University of Vienna).

in **Sec. II**, the *ShuttlePump* is a valveless pulsatile blood pump based on a Linear-Rotary Actuator (LiRA). With its combined linear-rotary motion, the specially-shaped piston of the *ShuttlePump* is responsible for opening/closing the pump's inlets and outlets while pumping blood in the systemic/pulmonary circulations. The fluid-dynamic, clinical and physiological aspects of the *ShuttlePump* have been studied at Charité Berlin and the Medical University of Vienna, proposing a working blood pump concept [7]. However, in order for the pump to operate in practice, it is necessary to design and realize its *drive system*, consisting of the power electronics (inverter and control) unit and the electric machine itself.

The main challenge is defining an actuation concept capable of meeting the required specifications in the least volume, as compactness is a requirement of utmost importance for an implantable TAH. Furthermore, the power losses of the LiRA must be minimized, in order to prevent blood damage (protein denaturation and aggregation) due to excessive heating. Finally, the combined linear and rotary motion has to be precisely controlled and synchronized in order to achieve proper pumping operation. This requires appropriate contactless position sensors [8], that also have to be fitted in the volume of the pump.

This paper discusses in detail the analysis, design, realization and experimental verification of the Linear Actuator

(LA) part of the *ShuttlePump*, which is an important interim result before continuing the research work with the design, realization and experimental analysis of the Rotary Actuator (RA) part and the final closed loop operation of the full LiRA.

The paper is structured as follows. **Sec. II** introduces the *ShuttlePump* in more detail, explaining its operating principle and highlighting the system requirements and stringent design constraints. **Sec. III** presents the machine analysis, topology selection and dimensioning based on which the optimization of **Sec. IV** is conducted. This finally leads to the selection of a candidate LA design. **Sec. V** introduces the realized hardware prototype of the LA and the test bench used for the experimental verification. The measurements are presented and commented in **Sec. VI**. Finally, **Sec. VII** concludes the paper.

II. OVERVIEW OF THE SHUTTLEPUMP TAH

This section explains the operating principle of the *ShuttlePump*, in order to understand why a LiRA is needed to make it work. Furthermore, the requirements of the drive system to be designed are introduced and discussed.

A. Operating Principle

As shown by **Fig. 1** and the yz -cut view of **Fig. 2 (a)**, the *ShuttlePump* consists of a cylindrical piston with a special curved shape at its two axial ends and a sealed enclosure with two inlets and two outlets. **Fig. 2 (b)** illustrates the pump's operating principle. The piston divides the enclosure into two chambers, serving as left and right heart ventricles, and has to simultaneously move along and rotate about the axial direction z . With the linear motion blood is pumped out of one chamber and new blood is collected in the other. The rotary motion instead controls the opening and closing of the inlets and outlets. This way, the blood flow is interrupted and hence no valves are needed, thus improving the durability and reducing complexity of the device with a single moving part. Moreover, compared to rotary blood pumps with a fast spinning impeller, this physiological, pulsatile flow featuring low velocities may reduce blood damage. As an additional feature, the piston is designed to be radially supported by the blood itself during operation, avoiding contact with the pump enclosure. This hydrodynamic journal bearing [9] is established by continuous rotation of the piston at a frequency of at least 1.5 Hz. This self-bearing feature not only extends the lifetime of the device, but also reduces the risk of thrombosis and similar adverse events that are usually related to the use of mechanical bearings in blood pumps [10], [11].

B. Drive System Requirements

The design of the drive system for the *ShuttlePump* needs to be carried out taking into account several important constraints and requirements. A complete list is available in **Tab. I** and some of the most relevant ones are discussed in the following.

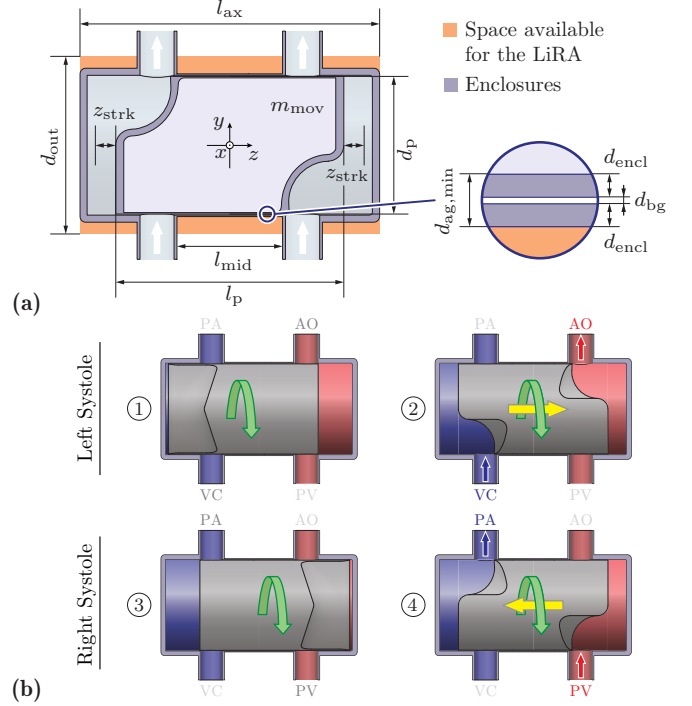


Fig. 2: (a) yz -cut view of the *ShuttlePump*, showing its enclosure and specially-shaped piston with annotated dimensions, reported in **Tab. I**. The orange area indicates the available space that can be used to fit the LiRA. A detailed view of the gap between enclosure and piston is shown on the right side. (b) Cut views of the *ShuttlePump* showing its operating principle. The linear motion pushes the blood in and out of the pump, whereas the rotary motion controls opening/closing of the inlets/outlets and enables the hydrodynamic bearing.

TABLE I: Specifications of the *ShuttlePump*.

Name	Symbol	Value	Unit
Maximum axial dimensions	l_{ax}	105	mm
Maximum radial dimensions	d_{out}	70	mm
Piston axial length	l_p	78	mm
Piston outer diameter	d_p	48.72	mm
Inter- in-/outlets distance	l_{mid}	40	mm
Enclosure thickness (lateral)	d_{encl}	0.5	mm
Blood gap	d_{bg}	140	μ m
Magnetic gap	$d_{ag,min}$	1	mm
Maximum axial force	$F_{req,peak}$	≈ 43	N
Axial torque	M_{req}	3.1	mNm
Max. allowed radial force	$F_{rad,max}$	25	N
Piston weight	m_{mov}	< 300	g
Piston frequency	f_{op}	1.5 - 5	Hz
Operating conditions		2.5 - 9	L/min
		50 - 160	mmHg
Maximum av. cont. losses	$P_{tot,avg,max}$	10	W
Blood temperature increase	ΔT_{max}	2	K

1) *Spatial Constraints:* The first important set of requirements are the spatial constraints imposed by the pump geometry and the maximum allowed external dimensions in order to guarantee that the final system is implantable. As it can be noticed from **Fig. 2 (a)**, the available space that can be occupied by the stator(s) of the LiRA is limited axially to $l_{ax} = 105$ mm and radially to a maximum outer diameter of $d_{out} = 70$ mm. Furthermore, the presence of the inlets and outlets limits even further the available space on the lateral surface of the enclosure. To ensure the manufacturability

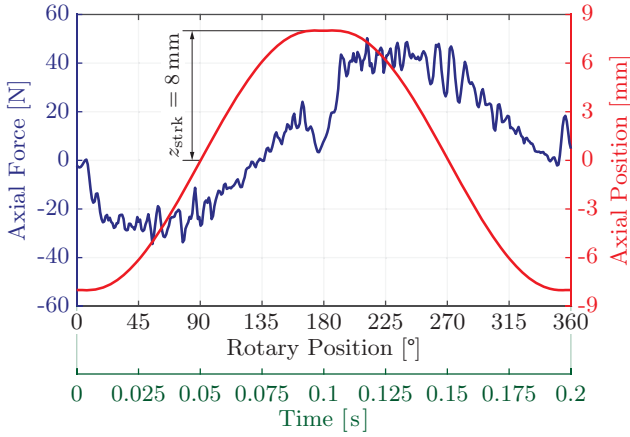


Fig. 3: Linear (axial) motion profile to be followed by the piston of the *ShuttlePump*. During motion, the required force profile F_{req} has to be provided to generate the necessary pressure at the cannula of the pump. The force profile is obtained by means of CFD simulations [7].

and sufficient rigidity of the enclosure, the thickness of its lateral wall cannot be smaller than $d_{\text{encl}} = 0.5$ mm. The same constraint applies to the external shell of the piston that is needed to prevent direct contact of the bare mover with the blood, which is clearly not allowed. The resulting minimum magnetic gap is hence $d_{\text{ag,min}} = d_{\text{encl}} + d_{\text{shell}} = 1$ mm. In addition, the thickness of the blood gap d_{bg} between the enclosure and the piston shell has to be considered. This key parameter plays an important role both for the hydrodynamic bearing, the shear stresses on the blood cells and the heating of the blood. Its value is optimized by means of Computational Fluid Dynamic (CFD) simulations at the *Medical University of Vienna* and selected to be $d_{\text{bg}} = 140$ μm [7].

2) *Motion Profile:* One of the most important requirements for proper operation is that the piston tracks the motion profile of **Fig. 3**, while complying to the required axial force profile F_{req} . The (continuous) torque requirement to keep the piston rotating in blood with $f_{\text{op}} = 5$ Hz is estimated by CFD simulations to be $M_{\text{req}} = 3.1$ mNm. The linear trajectory follows a quasi-sinusoidal profile shuttling around the middle of the enclosure with a stroke amplitude of $z_{\text{strk}} = 8$ mm. As the hydraulic resistance of the systemic circulation is higher than for the pulmonary circulation, the afterload pressure during the left systole is higher than during the right systole, which explains the asymmetric profile of F_{req} obtained from the CFD simulations. A higher linear force, with a peak of $F_{\text{req,peak}} \approx 43$ N is hence needed when traveling from the right chamber towards the left one.

3) *Power Losses:* Another crucial constraint is on the maximum allowed total losses of the LiRA, since they cause heating of the blood in the pump. In order to prevent blood damage, the increase of the blood temperature must be kept below the critical threshold of $\Delta T_{\text{max}} = 2$ K (i.e. the temperature must be below $T_{\text{max}} = 39^\circ\text{C}$) at any local part of the pump. The blood flow through the pump serves as forced convection cooling for the system. Nevertheless, the region in the middle, between inlets and outlets, is the most critical. In fact, due to the thin blood gap, there is only a

small blood volume between piston and enclosure that can heat up rapidly. Considering the worst case that all the losses coming from the LiRA are concentrated in this region and assuming that the heat is completely transferred to the blood, it is calculated that the average power losses over one period of operation should not exceed $P_{\text{tot,avg,max}} = 10$ W.

4) *Radial Forces:* According to the results of the CFD simulations for the hydrodynamic bearing design and with the selected blood gap thickness $d_{\text{bg}} = 140$ μm , it is decided to allow a maximum radial load of $F_{\text{rad,max}} = 25$ N. In order not to disturb further the hydrodynamic bearing, the design of the LiRA should preserve axial symmetry as much as possible. In fact, an asymmetric placement of the stator(s) could lead to excessive tilting of the piston during operation due to unbalanced reluctance forces between the PMs of the mover and the stator(s).

5) *Piston's Mass:* Finally, another aspect to consider is the total mass of the piston, which should be minimized. This not only reduces the inertial force required to accelerate it during axial motion, but also the reaction forces on the stator. This way, the stress on the tissues surrounding the implant is also beneficially reduced. The mass of the piston mostly consists of the mass of the mover of the LiRA, and will hence be indicated with m_{mov} .

III. MACHINE ANALYSIS AND DIMENSIONING

The machine design and optimization of the LA is based on a preliminary analysis, presented in this section. The goal is to select the most suitable motor concept for the LA given the stringent constraints discussed in **Sec. II-B** and identify the most important parameters affecting force generation, before continuing with a detailed FEM optimization.

A. LiRA Concept: Independent Actuators

The first decision taken is to realize the LiRA of the *ShuttlePump* as two independent actuators, i.e. a LA and a RA. This choice is motivated by a few important aspects. Simplicity and reliability are highly desirable features for a drive system, even more for an implantable blood pump. The higher the overall system's complexity, the higher the risk of partial failure with potentially very serious consequences for the patient. Also the practical realization of a complicated machine topology could get particularly challenging, especially under tight spatial constraints. When it comes to highly integrated LiRAs, for instance, the system's complexity can considerably increase [12]–[15]. Having many stator phase currents to supply and control independently is hardly advantageous. In fact, the inverter and control unit gets increasingly complicated as well and occupies a larger volume. This could be an issue, in case it is desired to implant it together with the blood pump. If that is not the case, a percutaneous driveline is needed to connect the implanted pump to the extracorporeal inverter and control unit. Even then, a large number of phase currents and control signals is not ideal, as the connecting driveline would increase in cross section. Therefore, it is highly beneficial to

minimize the number of phase currents of the LiRA as much as possible. In the literature, there are interesting concepts that follow this direction. One example is the screw motor, for which the linear motion is obtained passively with a special arrangement of the PMs [16]. By making one of the two motions passive, i.e. caused solely by reluctance forces, it is possible to only use three phase currents. Nevertheless, a solution of this kind hardly complies with the force requirements and motion profile of the *ShuttlePump*. Another aspect that motivates a separate design of the two actuators is that the required (average) mechanical output power of the LA is substantially larger than the RA. For the LA, starting from the motion profile and required force of Fig. 3, it can be calculated that $P_{\text{mech,avg,LA}} = 3.6 \text{ W}$. For the RA instead, due to the low rotational speed and torque, it is only needed to provide about $P_{\text{mech,avg,RA}} = 100 \text{ mW}$. By assuming that both actuators can be designed with the same power density, the volume share of the LA over the total LiRA volume is

$$V_{\text{share,LA}} = \frac{P_{\text{mech,avg,LA}}}{P_{\text{mech,avg,LA}} + P_{\text{mech,avg,RA}}} = 97.3 \%. \quad (1)$$

Therefore, it is reasonable to use as much space as possible for the LA and provide the best actuator design possible, e.g. by avoiding a combined LiRA concept that could significantly reduce the LA's efficiency. The LA is then realized as a Tubular Linear Actuator (TLA). This way, the full lateral surface of the cylindrical piston can be used for axial force generation. The TLA is implemented as a Permanent Magnet Synchronous Machine (PMSM), which is a typical choice for blood pumps [17]. In fact, PMs allow to reach high flux densities in the least volume, thus meeting the compactness requirements of such implantable devices.

B. PMSM Topology Selection for the TLA

The most suitable machine topology for the (T)LA is selected among a variety of alternatives. The first and most basic decision to take is on the poles/slots combination. With a number of stator slots $N_s = 6$ and a number of mover poles $N_p = 2$, it is possible to maximize the winding factor to $\xi = 1$. This is achieved with a distributed winding, which for a TLA can be conveniently realized with 6 individual circular coils.

For the stator, it is possible to choose either a slotted (cf. Fig. 4 (a)) or a slotless (cf. Fig. 4 (b)) design. With a slotted stator with stator teeth, the magnetic air gap length can be minimized to $d_{\text{ag,min}} = 1 \text{ mm}$, which results in a higher air gap flux density and hence a higher force constant compared to a slotless stator, where the air gap length and resulting force constant is mainly defined by the stator winding thickness (which should be maximized to minimize the winding losses). Furthermore, a slotless stator presents little variations in the air gap reluctance along the axial direction, which considerably mitigates cogging effects (cf. Sec. III-C). For these reasons, both designs are considered in the subsequent FEM optimization of Sec. IV.

For what concerns the mover, the needed poles can be obtained with two different PM arrangements [18]. One option is to use Surface-mounted PMs (SPM) with a radial magnetization direction, as shown in Fig. 4 (c). As it can

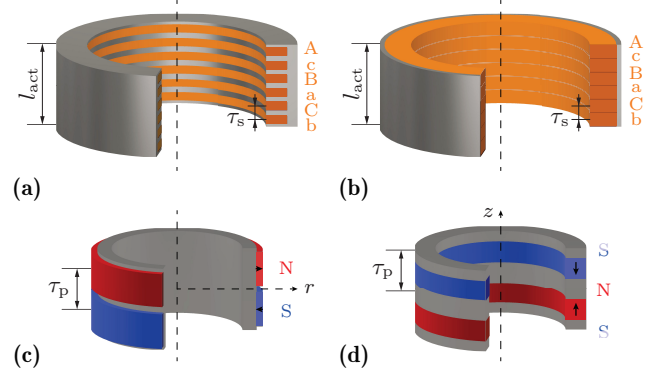


Fig. 4: Considered options for the stator and the mover of the TLA for the case of $N_s = 6$ stator slots and $N_p = 2$ mover poles. (a) Slotted stator, (b) slotless stator, (c) SPM mover with radially (r -) magnetized PMs and (d) IPM mover with axially (z -) magnetized PMs.

be noticed, this requires a mover back iron to close the magnetic path with the minimum length. To realize this in practice, custom-made radially-magnetized PMs are required, which have extremely high manufacturing costs. Nevertheless, it is possible to obtain approximately the same result with smaller PM segments. The other option is to use Interior PMs (IPM) with an axial magnetization direction, interleaved by rings of ferromagnetic material as shown in Fig. 4 (d). These magnets are considerably easier to produce and the mover can be assembled by stacking the ring-shaped PMs and the ferromagnetic rings together. Finally, one further option would be the Halbach array. However, due to difficult realization, this is not investigated further.

C. Variable Air Gap Reluctance Effects

Besides the selection of the basic machine topology, there are three important air gap reluctance effects that have to be considered to design a working TLA. These effects are much more prominent (and critical) with a small magnetic air gap length, which is the case for a slotted stator design. The first effect is the radial magnetic attraction force acting on the mover. This appears as soon as its axis is not aligned to the stator's one. In fact, it can be shown that the center of the stator is an unstable equilibrium position for the mover. As soon as this is displaced radially, the reluctance forces caused by the attraction of the PMs with the stator core are not anymore balanced, with a resulting radial magnetic pull (cf. Fig. 5 (a) and (b)). As the *ShuttlePump* has no mechanical bearing holding the mover perfectly concentric, this force can heavily disturb the hydrodynamic bearing and should hence be explicitly considered in the optimization.

The second effect is the cogging force along the axial direction, appearing for slotted stator designs. This is caused by the variable air gap reluctance profile due to the presence of the stator teeth [19]. It is known that the profile of the cogging force F_{cogg} along the axial direction z exhibits a spatial periodicity given by the least common multiple of the number of stator slots N_s and the number of mover poles N_p ,

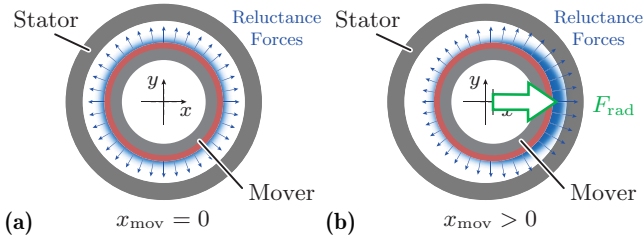


Fig. 5: Radial magnetic attraction force effect. (a) With a centered mover, all the radial reluctance forces are balanced, whereas (b) when the mover is displaced radially (e.g. along the x -direction), a net radial attraction force F_{rad} appears. Note that the mover is not to scale on purpose to better visualize the reluctance forces.

i.e.

$$F_{\text{cogg}} = \hat{F}_{\text{cogg}} \sin\left(\frac{N_{\text{cogg}} \pi}{\tau_p} z\right) \text{ with } N_{\text{cogg}} = \text{lcm}(N_s, N_p). \quad (2)$$

with $\tau_p = l_{\text{act}}/N_p$ the pole pitch and l_{act} the length of the actuator. If no counter measure is taken, the amplitude \hat{F}_{cogg} can be so large as to compromise the operation of the TLA. The most effective way to mitigate cogging force is to use pole shoes, as they smooth out the air gap reluctance profile [20], [21]. Therefore, for slotted stator designs, pole shoes will be included in the optimization as well.

The last important effect to consider is the edge effect or edge cogging force. Also this is caused by the air gap reluctance. More precisely, when the mover is displaced axially away from the center position as in **Fig. 6 (a)**, the total reluctance seen by the PMs sharply increases, as there is no stator in front. Consequently, there is a strong axial force $F_{\text{ax,edge}}$ that pulls the mover back towards the center position, i.e. to the condition with minimum reluctance. This can be countered by extending either the stator (**Fig. 6 (b)**) or the mover (**Fig. 6 (c)**) along the axial direction in such a way that the total reluctance is approximately constant during the whole axial motion [18]. In order to minimize the mass of the mover, the former option is preferred, i.e. the stator is extended by $2 \cdot z_{\text{strk}} = 16 \text{ mm}$. Depending on the size of a stator pitch $\tau_s = l_{\text{act}}/N_s$, it would be possible to fit additional coils in the stator extensions, as e.g. visible in **Fig. 6 (b)**. However, energizing such coils would generate additional ohmic losses which do not fully contribute to force generation. For this reason, no further coil is added in the stator extensions. As

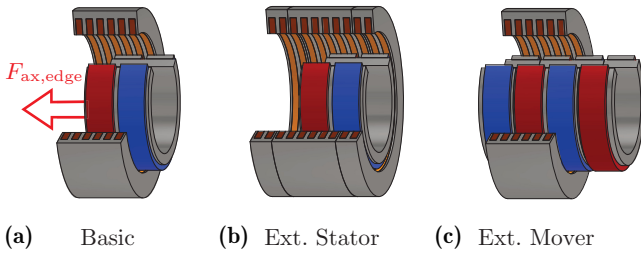


Fig. 6: Edge cogging force effect and possible solutions. (a) Basic TLA with stator and mover of equal length, for which a strong edge cogging force $F_{\text{ax,edge}}$ appears (magnetic spring) as soon as the mover is displaced from the center of the actuator. (b) Solution 1: TLA with extended stator. The stator extensions can optionally host additional stator coils. (c) Solution 2: TLA with extended mover.

a consequence, it is important to notice that the active length (and hence area) effectively contributing to force generation drops when the mover is displaced from the center of the actuator, i.e.

$$l_{\text{act,eff}}(z_{\text{mov}}) = l_{\text{act}} - |z_{\text{mov}}| \quad (3)$$

where z_{mov} is the position of the mover. In future work, the stator extensions will be used to integrate the RA for a highly compact design.

D. Analysis and Dimensioning from First Principles

Before proceeding with the FEM optimization of the TLA, a short preliminary analysis based on first principles is conducted. This is useful for multiple reasons. First, it enhances the understanding and the interpretation of the subsequent optimization results. Furthermore, it allows to fix some parameters beforehand by understanding their effect, thus reducing the number of optimization variables to sweep. Last but not least, it can be used for a feasibility check, i.e. to roughly estimate whether the required force can be achieved respecting the provided constraints on power losses and dimensions.

For internal force generation in AC machines, consider the area-related force density,

$$\sigma_{\text{ax}}(z) = S(z) B_{\text{ag}}(z), \quad (4)$$

where $S(z)$ is the equivalent current sheet and $B_{\text{ag}}(z)$ the magnetic flux density in the air gap at the position z (assuming symmetric axisymmetric designs). The total axial force F_{ax} is obtained by integrating $\sigma_{\text{ax}}(z)$ along the active area, i.e. the (inner) lateral surface of the cylindrical TLA, hence

$$F_{\text{ax}} = 2\pi r_{\text{mov}} \int_{-l_{\text{act}}/2}^{l_{\text{act}}/2} \sigma_{\text{ax}}(z) dz. \quad (5)$$

With $N_p = 2$, i.e. one pole pair, only the fundamental components of $B_{\text{ag}}(z)$ and $S(z)$ contribute to force generation. Therefore, (5) can be rewritten as

$$F_{\text{ax}} = 2\pi r_{\text{mov}} \int_{-l_{\text{act}}/2}^{l_{\text{act}}/2} S_1(z) B_{\text{ag},1}(z) dz. \quad (6)$$

The fundamental component $B_{\text{ag},1}(z)$ can be written as

$$B_{\text{ag},1}(z) = -\hat{B}_{\text{ag},1} \sin\left(z \frac{2\pi}{l_{\text{act}}} + \vartheta_{\text{mov}}\right), \quad (7)$$

where $\vartheta_{\text{mov}} = -z_{\text{mov}} \frac{2\pi}{l_{\text{act}}}$ is the electrical angle of the mover (with respect to the stator). The amplitude $\hat{B}_{\text{ag},1}$ can be approximated from the equivalent magnetic circuit model of **Fig. 7 (a)**. The circuit is valid for the SPM case and it is greatly simplified. It considers only the radial field component of the main flux path, thus neglecting any leakage flux. Moreover, it assumes that the field is homogeneous and does not consider any fringing due to the large coverage of the pole shoes. With these assumptions, the peak air gap flux density is

$$\hat{B}_{\text{ag}} = \frac{\phi_{\text{ag}}}{A_{\text{ag}}} = \frac{\theta_{\text{PM}}}{\mathcal{R}_{\text{ag,tot}} A_{\text{ag}}} = \frac{H_c d_{\text{PM}} \mu_0}{d_{\text{ag}} + d_{\text{PM}}}, \quad (8)$$

where ϕ_{ag} is the magnetic flux in the air gap, A_{ag} the air gap cross section, θ_{PM} the magnetomotive force generated by one

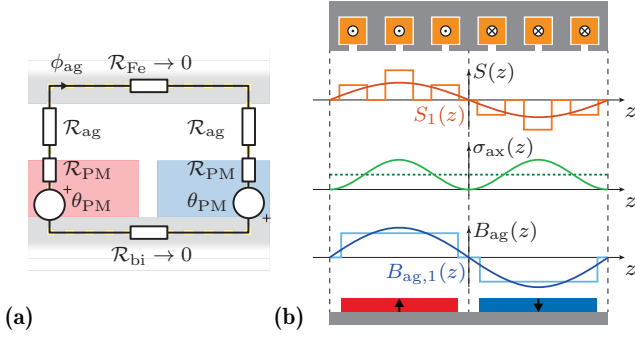


Fig. 7: (a) Simplified equivalent magnetic circuit at the air gap of the LA, valid for the SPM case. The field is assumed to be homogeneous in the radial direction and any leakage and fringing is neglected. It is assumed that the magnetic permeability of the cores is $\mu_{r,Fe} \rightarrow \infty$, from which $\mathcal{R}_{\{Fe,bi\}} \rightarrow 0$. (b) Exemplary machine plan for the analysis of force generation, showing the equivalent current sheet $S(z)$ and its fundamental component $S_1(z)$, the area-related force density $\sigma_{ax}(z)$ and the air gap magnetic flux density $B_{ag}(z)$ and its fundamental component $B_{ag,1}(z)$.

PM with coercivity H_c and $\mathcal{R}_{ag,tot}$ the total equivalent air gap reluctance. The amplitude of the first harmonic $\hat{B}_{ag,1}$ also depends on the PM coverage factor k_{PM} (that determines the length of and hence the gap between the PMs) and is

$$\hat{B}_{ag,1} = \frac{4}{\pi} \hat{B}_{ag} \sin\left(k_{PM} \frac{\pi}{2}\right). \quad (9)$$

The current sheet $S(z)$ is obtained considering the currents impressed in the distributed winding as shown in the exemplary machine plan of **Fig. 7 (b)**. The fundamental component $S_1(z)$ can be written as

$$S_1(z) = -\hat{S}_1 \sin\left(z \frac{2\pi}{l_{act}} + \vartheta_{stat}\right), \quad (10)$$

where ϑ_{stat} is the electrical angle of the stator field, which can be controlled with the inverter to be $\vartheta_{stat} = \vartheta_{mov}$ for maximum force generation (Field-Oriented Control, FOC). The amplitude \hat{S}_1 is calculated as

$$\hat{S}_1 = \frac{6 \sin\left((1 - k_{FeCu}) \frac{\pi}{6}\right) N \hat{I}}{\left((1 - k_{FeCu}) \frac{\pi}{6}\right) l_{act}}, \quad (11)$$

where $N \hat{I}$ is the peak Atturns impressed in the stator winding and the iron-to-copper ratio parameter k_{FeCu} is introduced. As in a slotted design the width of a tooth and a coil add up to a stator slot pitch $\tau_s = l_{act}/6$, it holds $l_{Fe} = k_{FeCu} \tau_s$ and $l_{Cu} = (1 - k_{FeCu}) \tau_s$. With this definition, for the special case $k_{FeCu} = 0$ a slotless stator design is obtained.

By integrating (6) and with the expressions for the fundamentals (7) and (11), the axial force results finally as

$$F_{ax} = \pi l_{act} r_{mov} \hat{S}_1 \hat{B}_{ag,1} = \frac{1}{2} A_{act} \hat{S}_1 \hat{B}_{ag,1}, \quad (12)$$

where $A_{act} = 2\pi r_{mov} l_{act}$ is the active area of the LA. The corresponding total ohmic losses of the stator winding are

$$P_{Cu} = 3 R_0 (N \hat{I})^2 = 3 \frac{l_{w,0}}{\sigma_{Cu} k_{ff} A_{Cu,0}} (N \hat{I})^2, \quad (13)$$

where R_0 is the single-turn resistance of a circular coil, $l_{w,0}$ is the single-turn length of the coil, σ_{Cu} is the conductivity

of copper, k_{ff} the fill factor and the single-turn copper cross section is

$$A_{Cu,0} = d_{Cu} l_{Cu} = d_{Cu} (1 - k_{FeCu}) (l_{act}/6). \quad (14)$$

The derived first-principles relations offer some meaningful insights on which variables contribute to force generation and/or ohmic losses. For instance, from (8), (9) and (12) one can recognize the role of the air gap length d_{ag} , which should be minimized to maximize F_{ax} . In the denominator of (8), one can observe the effect of the series reluctance of the PMs (with thickness d_{PM}) in a SPM mover. Most importantly, from (13) and (14) it can be seen that maximizing the fill factor k_{ff} and the coil copper cross section $A_{Cu,0}$ is crucial to reduce the ohmic losses. As a consequence, the available TLA volume should be maximally used. Hence it is already possible to fix $d_{out} = 70$ mm, thus maximizing d_{Cu} . Also the iron-to-copper ratio k_{FeCu} directly affects the ohmic losses for (almost) the same output force (the effect in (11) is minimal) and should be ideally minimized. Nevertheless, care must be taken and further investigation is needed. In fact, very thin stator teeth are not only mechanically more fragile and difficult to manufacture, but also prone to magnetic saturation. Furthermore, recall that the simplified magnetic circuit model holds for a large shoe coverage with homogeneous field and does not include fringing and leakage effects.

Finally, (14) reveals that also the actuator's length l_{act} should be maximized as far as possible. Another strong motivation is given by the (effective) active length of the extended stator design found in (3). The larger l_{act} , the smaller the reduction of $l_{act,eff}(z_{mov})$ during the axial motion. Furthermore, recall that the thin layer of blood serving as hydrodynamic bearing can heat up very easily by absorbing the heat generated by the LiRA. If the actuator is longer, the volume of such blood layer is larger, and hence its temperature increase is smaller for the same power losses. With the chosen extended stator design the total stator length is $l_{stat} = l_{act} + 2 \cdot z_{strk}$. As the length between left and right inlets/outlets is limited to $l_{mid} = 40$ mm, the actuator's length is finally maximized to $l_{act} = 24$ mm.

The preliminary analysis is completed with one last consideration on the radial attraction force F_{rad} . Being a reluctance force, it depends linearly on the active area and quadratically on the air gap magnetic flux density, i.e.

$$F_{rad} \propto A_{act} B_{ag}^2. \quad (15)$$

Recall that F_{rad} should be limited in order not to impair the hydrodynamic bearing. In contrast, for force generation (cf. (12)) high values of B_{ag} and A_{act} are desirable. For the same output force F_{ax} , a reduced B_{ag} would need to be compensated with increased current $N \hat{I}$ or a larger active area A_{act} . Between the two options, increasing A_{act} is more favorable, as a larger current increases quadratically the ohmic losses (cf. (13)). With the maximized length $l_{act} = 24$ mm and hence fixed A_{act} , the trade-off between radial attraction force F_{rad} and ohmic losses P_{Cu} becomes the main focus of the subsequent optimization, from which a Pareto-front has to be expected.

IV. FEM MACHINE OPTIMIZATION

This section discusses the FEM optimization conducted on a 2D parameterized model of the candidate TLA topology. The trade-offs that appear by exploring the design space are highlighted, leading to the selection of the final design.

A. 2D FEM Model

A TLA can be conveniently studied with a 2D axisymmetric FEM model. However, this does not allow to investigate the radial attraction forces, as they only appear when the mover and stator axes are misaligned. Therefore, a 2D Cartesian model (i.e. with no assumed symmetry) is used instead, comprising the full cross-section of the TLA as shown in **Fig. 8 (a)**. This way, it is possible to obtain both the axial and radial forces acting on the mover with a single magnetostatic 2D model, avoiding to use a 3D one with considerably higher simulation effort. Nevertheless, it is necessary to verify that the results of the 2D Cartesian model approximate well the ones from the corresponding 2D axisymmetric or 3D models. Specifically, the results from the 2D Cartesian model need to be scaled correctly, as shown further, as they are returned per 1 m of length along the y -direction.

1) *Model Definition:* The model is parameterized as indicated in **Fig. 8 (a)**. In order to keep the simulation effort to a minimum, the materials used in the model are simplified. The stator core and the mover back iron are made of a linear, ferromagnetic material with $\mu_r = 4000$ and negligible electrical conductivity. Consequently, the results have to be checked for potential magnetic saturation of the material, that occurs in practice for too high values of the B field (e.g. > 1.6 T for electrical steel). The coils are modeled with a solid copper cross section, i.e. with a single turn, for simplicity. In order to take into account a realistic fill factor of $k_{ff} = 0.6$, the copper material is modeled with a reduced conductivity $\sigma_{Cu,ff} = k_{ff} \sigma_{Cu} = 3.4 \text{ MS m}^{-1}$. Finally, for the PMs a coercivity $H_c = 1000 \text{ kA m}^{-1}$ is assumed, which approximately corresponds to the N50 magnetization grade of commercial NdFeB PMs. As a Cartesian model is used, the magnetization direction is along the x -axis. In order to obtain the correct machine constant, the current excitations are assigned to the coils as indicated in **Fig. 8 (a)**. In particular, the electrical angle ϑ is tied to the axial position of the mover z_{mov} in order to generate the maximum force per ampere (MFPA) with FOC for all axial positions. This way $N\hat{I}$ corresponds effectively to the amplitude of the force-generating q -current component.

2) *Simulation Outputs and Scaling:* The outputs of the magnetostatic 2D FEM simulations needed for the subsequent machine optimization are the maximum radial attraction force $F_{rad,max}$, the axial force F_{ax} generated for the current amplitude $N\hat{I}$ (from which the machine force constant $k_m = F_{ax}/\hat{I}$ can be derived) and the corresponding ohmic losses P_{Cu} in the winding. High-frequency-copper losses are neglected since the machine will be fed by an inverter with LC -output filter, providing quasi-sinusoidal low-frequency currents. Due to the low-frequency operation, also the core losses P_{Fe} are neglected in a first step. For the maximum radial attraction

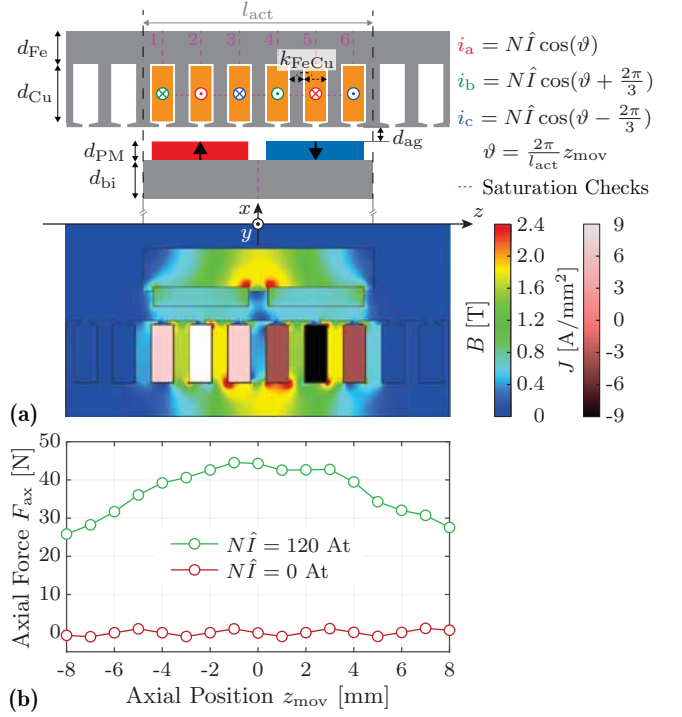


Fig. 8: (a) 2D FEM Cartesian model of the TLA for an exemplary design, with indicated parameters in the upper half and solved B and J fields in the bottom half (*Ansys Maxwell*). By modeling the full section of the TLA, it is possible to obtain both axial and radial forces acting on the mover with one model. **(b)** Exemplary axial force profiles for the cases $N\hat{I} = 120 \text{ At}$, giving the total axial drive force $F_{ax}(z)$ and $N\hat{I} = 0 \text{ At}$, giving the axial cogging force component $F_{cogg}(z)$.

force $F_{rad,max}$, the mover is displaced in the x -direction by $x_{mov} = d_{bg} = 140 \mu\text{m}$. The simulation returns a force per unit length (i.e. 1 m) $F_{x,sim}$ acting on the mover along the x -direction. By comparing it with the results of the corresponding 3D FEM simulations, it is found that the total radial force is well-approximated (matching within 1.5 %) as

$$F_{rad} = (\pi r_{mov}/2) F_{x,sim}, \quad (16)$$

i.e. with a scaling factor equal to a quarter of the mover circumference. Similarly, the generated axial force per unit length $F_{z,sim}$ is compared to both the corresponding axisymmetric 2D and 3D FEM simulations. In this case, the scaling factor corresponds to half of the mover circumference, hence the total axial force is

$$F_{ax} = (\pi r_{mov}) F_{z,sim}, \quad (17)$$

which matches within 1.4 % to the results of the 2D axisymmetric model and 2.4 % for the 3D. Note that $F_{z,sim}$ is obtained for the case $x_{mov} = 0$, i.e. for a radially centered mover. The two scaling lengths used in (16) and (17) can be explained as follows. As the axial force acts in the same way over the whole mover circumference, the full 3D results are obtained by revolving the Cartesian 2D model by 180° . The radial attraction forces instead are not acting equally along the whole circumference, as already sketched in **Fig. 5 (b)**. It can be approximated that the components acting along the top and bottom quarter of circumference cancel each other out and only the ones acting on the left and right sides contribute.

If the parameter z_{mov} is varied in the range $[-z_{\text{strk}}, z_{\text{strk}}]$, the axial force profile in **Fig. 8 (b)** is obtained. As expected from (3), the generated force reduces approximately linearly with $|z_{\text{mov}}|$, as the active machine length $l_{\text{act,eff}}$ reduces. For a maximally displaced mover, i.e. $|z_{\text{mov}}| = z_{\text{strk}}$, the generated force is only about $1 - |z_{\text{strk}}|/l_{\text{act}} = 2/3$ of the maximum force $F_{\text{ax,max}} = F_{\text{ax}}(z_{\text{mov}} = 0)$. For $N\hat{I} = 0$, only the cogging force component F_{cogg} appears, also reported in **Fig. 8 (b)**. Thanks to the pole shoes, its amplitude is small, i.e. only $\hat{F}_{\text{cogg}} \approx 1$ N.

The FEM simulation also returns the ohmic losses in the LA winding. These are obtained for the assigned currents i_a , i_b and i_c with $N\hat{I}_{\text{test}} = 120$ Aturns in this exemplary case. This is the current amplitude needed to generate the peak force $F_{\text{req,peak}} = 43$ N and is hence not needed continuously during the whole operation period. Therefore, in order to find the (instantaneous) losses profile versus time $P_{\text{Cu}}(t)$, it is necessary to combine the required force profile $F_{\text{req}}(t)$ of **Fig. 3** with the obtained force profile from FEM $F_{\text{ax}}(z)$ in **Fig. 8 (b)**. In **Fig. 9 (a)**, $F_{\text{ax}}(z)$ is adapted versus time as $F_{\text{ax}}(t)$ according to the motion profile $z(t)$ in **Fig. 3** and shown for $N\hat{I}_{\text{test}} = 120$ Aturns. This way, the required current amplitude $N\hat{I}_{\text{req}}$ is determined as

$$N\hat{I}_{\text{req}}(t) = \frac{F_{\text{req}}(t)}{F_{\text{ax}}(t)} N\hat{I}_{\text{test}}. \quad (18)$$

and is exemplarily shown in **Fig. 9 (b)**, together with the resulting phase currents. From this and with the simulated single-turn resistance R_0 , one gets the losses profile

$$P_{\text{Cu}}(t) = 3 R_0 (N\hat{I}_{\text{req}}(t))^2 \quad (19)$$

reported in **Fig. 9 (c)**, of which the average $P_{\text{Cu,avg}}$ is considered.

B. Three-Steps Optimization Procedure

The parameterized 2D FEM model can now be used to perform the machine optimization. For this purpose, the model parameters are swept as reported in **Tab. II**. In order to keep the design space compact and avoid prohibitive simulation times, the parameters are divided into three groups and the optimization is performed in three steps. In a first preliminary step, the parameters k_{shoe} and k_{PM} are swept on a test design. As it will be shown, it is possible to fix them beforehand independently. In a second step, the main optimization parameters are swept. They are expected to have the most noticeable

TABLE II: Swept optimization parameters.

Name	Symbol	Range	Step	Unit
Group 1				
Shoe coverage	k_{shoe}	[0.5, ..., 0.9]	0.05	
PM coverage	k_{PM}	[0.6, ..., 0.9]	0.05	
Group 2 (Main)				
Magnetic gap length	d_{ag}	[1, ..., 2]	0.5	mm
PM thickness	d_{PM}	[1, ..., 3, 5]	0.5	mm
Copper layer thickness	d_{Cu}	[2, ..., 6]	1	mm
Iron-Copper ratio	k_{FeCu}	[0, ..., 0.8]	0.2	
Group 3				
Stator core thickness	d_{Fe}	[2, ..., 5]	0.5	mm
Back iron thickness	d_{bi}	[2, ..., 6]	0.5	mm

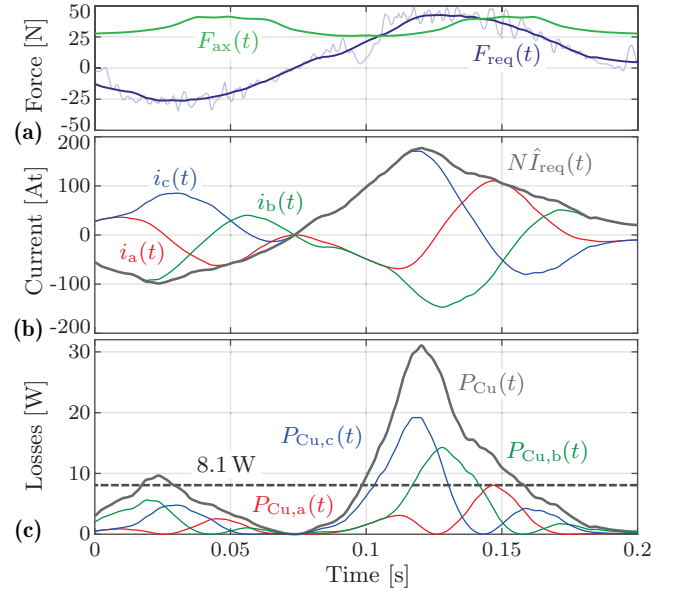


Fig. 9: (a) Comparison between the generated force $F_{\text{ax}}(t)$ for a fixed test current $N\hat{I}_{\text{test}} = 120$ Aturns as obtained from the FEM simulations and the required force profile from **Fig. 3**, here smoothened. (b) Required current amplitude $N\hat{I}_{\text{req}}(t)$ and resulting realistic (single-turn) phase currents $i_{\{a,b,c\}}(t)$. (c) Instantaneous ohmic losses $P_{\text{Cu},\{a,b,c\}}(t)$ corresponding to the currents in (b) for the simulated single-turn resistance $R_0 = 330 \mu\Omega$. The continuously dissipated power is the average of the total losses $P_{\text{Cu}}(t)$.

effects on the desired outputs and are hence explored in detail. Among these there is in fact the thicknesses of the permanent magnets d_{PM} , the copper layer d_{Cu} and the magnetic gap length d_{ag} , as well as the iron-to-copper ratio k_{FeCu} . Note that also the case $k_{\text{FeCu}} = 0$ is considered, which corresponds to the slotless stator designs. In a third step, i.e. after the main design space is obtained and a design is selected, the third group of parameters is adjusted. The thickness of the stator core d_{Fe} or of the mover back iron d_{bi} have a limited impact on the inspected outputs. They do not significantly change e.g. the generated force nor the reluctance forces, especially with the assumed linear magnetic material. Therefore, they are chosen only to guarantee that no magnetic saturation occurs in the stator nor the back iron. As these two parameters do influence the resulting mover mass and actuator volume, though, in the second step they are assigned as $d_{\text{Fe}} = d_{\text{bi}} = 2 d_{\text{PM}}$. The three-steps optimization procedure can be summarized by the diagram of **Fig. 10**.

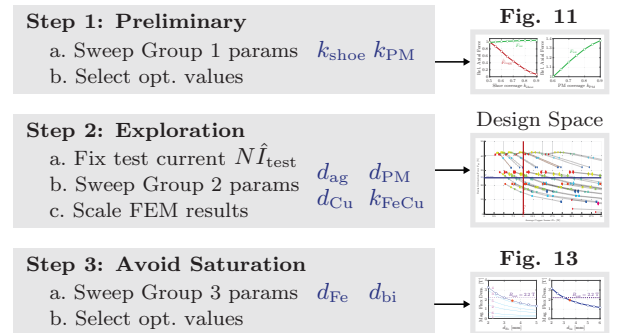


Fig. 10: Flow diagram showing the three-steps FEM-based optimization procedure of the TLA.

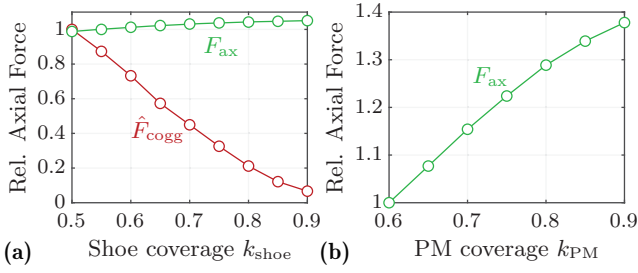


Fig. 11: Results of the first (preliminary) optimization step. (a) Effect of the shoe coverage factor k_{shoe} on the axial drive force F_{ax} and the cogging force amplitude \hat{F}_{cogg} , relatively to the case $k_{\text{shoe}} = 0.5$. (b) Effect of the PM coverage factor k_{PM} on the axial drive force F_{ax} , relatively to the case $k_{\text{PM}} = 0.6$.

C. Optimization, Design Space and Selected Design

The results from the first (preliminary) optimization step are reported in **Fig. 11**. As it can be seen in **Fig. 11 (a)**, the shoe coverage k_{shoe} has a limited impact on the generated axial force, but a clear beneficial effect in reducing the cogging force amplitude \hat{F}_{cogg} . Therefore, k_{shoe} should be selected as large as possible. However, note that if the distance between two pole shoe edges is comparable to the air gap length d_{ag} , fringing effects start to appear, which worsen the machine constant and should hence be avoided. For this reason, it is found by inspection of the FEM fields that $k_{\text{shoe}} = 0.8$ is an adequate choice. For what concerns k_{PM} , one can observe that the impact on the axial force is much more prominent, which is expected (see (9), **Fig. 7 (b)** and the discussion thereof in **Sec. III-D**). The only motivation to reduce k_{PM} is given by the very high magnetic flux density in the mover back iron, resulting if no gap is left between the PMs with opposite polarity. By inspection of the solved fields, a value around $k_{\text{PM}} = 0.8$ is reasonable. Finally, $k_{\text{PM}} = 0.83$ is chosen,

as this results in a PM length of $l_{\text{PM}} = 10$ mm, which is a convenient size to manufacture and/or to find commercially.

The design space generated by the second (main) optimization step with $3 \times 6 \times 4 \times 5 = 360$ parameter configurations is explored with the aid of **Fig. 12**. Each design is initially simulated with a fixed test current $N\hat{I}_{\text{test}} = 120$ Aturns, which results in a certain generated maximum axial force $F_{\text{ax,max}}$. For a direct comparison, the results of each design are then scaled to the same axial force output $F_{\text{req,peak}} = 43$ N. Such force is reached for a scaled current $N\hat{I}_{\text{scal}} = (F_{\text{req,peak}}/F_{\text{ax,max}})N\hat{I}_{\text{test}} = k_{\text{scal}}\hat{I}_{\text{test}}$, which implies that the average ohmic losses have to be scaled as $P_{\text{Cu,scal}} = k_{\text{scal}}^2 P_{\text{Cu}}$. In **Fig. 12**, the design space is visualized on the $P_{\text{Cu}}-F_{\text{rad}}$ plane, which represents the most relevant design trade-off. On this plane, it is also possible to distinguish quite clearly the effect of the swept parameters. The ‘magnetic’ parameters d_{ag} and d_{PM} have the most noticeable effect on both F_{rad} and P_{Cu} . This is expected, as they directly determine the magnetic flux density in the air gap B_{ag} (cf. (8)), with the consequent trade-off discussed in **Sec. III-D**. The designs can be conveniently divided according to the value of d_{ag} into three groups. Furthermore, the points sharing the same parameter configuration except for d_{PM} are connected. The magnetic gap length d_{ag} affects B_{ag} as it increases the equivalent reluctance of the magnetic circuit, with the result that the magnetic flux ϕ_{ag} is lower. The extreme case is represented by the group of slotless designs, which due to the absence of stator teeth have the largest magnetic air gap. Consequently, these designs exhibit very low radial attraction force, but also comparably high losses. For instance, the best slotless design can not achieve the required force with less than $P_{\text{Cu}} = 21.8$ W and only for very thick/heavy PMs ($d_{\text{PM}} = 5$ mm). The thickness d_{PM} instead affects B_{ag} by increasing the PM’s MMF $\theta_{\text{PM}} = H_c d_{\text{PM}}$, and

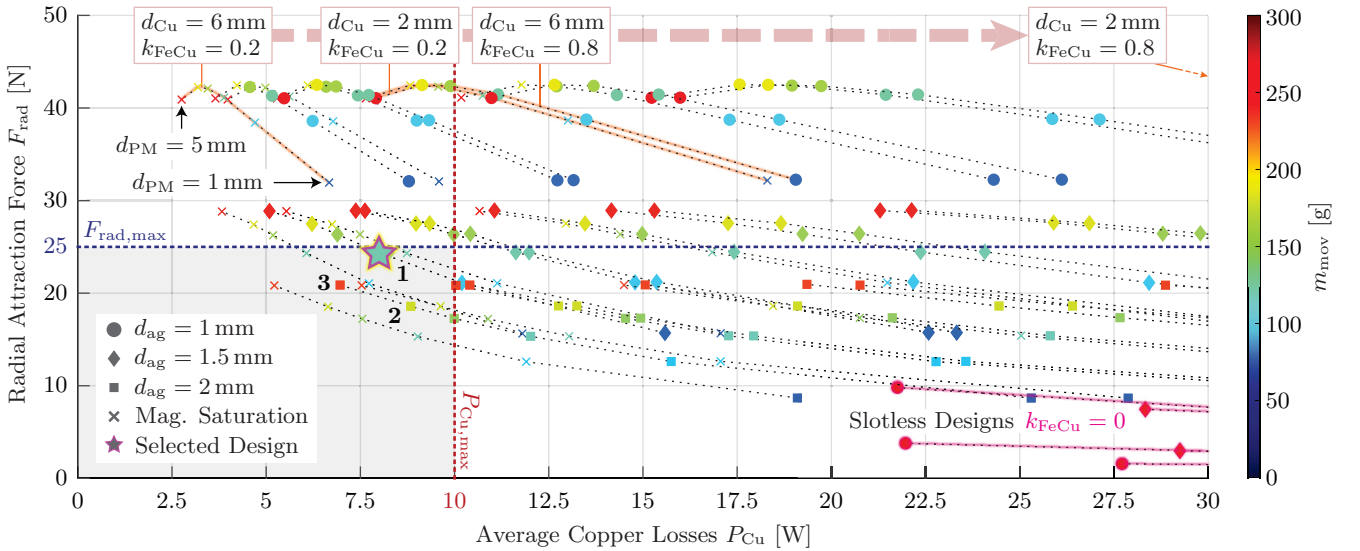


Fig. 12: Design space generated by the second optimization step, visualized on the $P_{\text{Cu}}-F_{\text{rad}}$ plane. The color of each point represents the mover mass m_{mov} . The points with the same parameters configuration except for d_{PM} are connected (see e.g. the dashed lines highlighted in orange). This helps to visualize the effect of the remaining swept parameters. The considered threshold for magnetic saturation is $B_{\text{sat}} = 2.2$ T. At the bottom-right corner, the slotless designs are visible (highlighted in magenta). Moreover, the limits in losses and radial attraction force are reported, which allow to identify the feasible designs 1, 2 and 3 listed in **Tab. III**.

TABLE III: Feasible LA designs under the specified constraints.

#	d_{ag}	d_{PM}	d_{Cu}	k_{FeCu}	F_{rad}	P_{Cu}	m_{mov}
1)	1.5 mm	2 mm	6 mm	0.4	24.4 N	8.0 W	129 g
2)	2 mm	3 mm	6 mm	0.4	18.6 N	8.8 W	174 g
3)	2 mm	5 mm	6 mm	0.4	20.9 N	7.0 W	241 g

hence the magnetic flux ϕ_{ag} . Nevertheless, it also introduces an equivalent series reluctance comparable to air ($\mu_r \approx 1.05$), which at a certain point counterbalances the increased MMF (cf. again (8)). The ‘copper-related’ parameters d_{Cu} and k_{FeCu} only affect P_{Cu} instead, as they determine the copper cross section $A_{Cu,0}$ (cf. (14)). For instance, consider a group of designs connected by a dashed line. Decreasing the value of d_{Cu} and/or increasing the value of k_{FeCu} decreases $A_{Cu,0}$ and hence scales the group towards the right along the P_{Cu} -axis. Clearly, there is two limits to consider in this regard. On one hand, d_{Cu} is limited by the maximum outer diameter of the LA (and also the thickness of the stator core d_{Fe} has to be included). On the other hand, smaller values of k_{FeCu} make the stator teeth thinner, to the point that the magnetic flux density is too high and the material saturates.

With the limit in average losses $P_{Cu,max}$ and radial attraction force $F_{rad,max}$ and by excluding the cases with magnetic saturation, only the three feasible designs listed in **Tab. III** remain. The design with the least copper losses and radial attraction force is *Design 3*. Nevertheless, the resulting mover mass is the highest. As the copper losses have to be minimized, but a radial attraction force up to the limit can be tolerated, *Design 1* is finally selected, which has almost half the mass.

With this choice, it is finally possible to complete the optimization with the third step, ensuring that no magnetic saturation occurs. The parameters d_{Fe} and d_{bi} are swept and the resulting average magnetic flux densities in the stator core (above every slot) and the mover back iron (in the middle) are shown in **Fig. 13**. It can be observed that it is possible to save volume and weight for both stator and mover by using a magnetic material with high saturation flux density, like e.g. *VACOFLUX50*. Considering the threshold $B_{sat} = 2.2$ T (with a little margin from it), the values $d_{Fe} = d_{bi} = 3.5$ mm are selected.

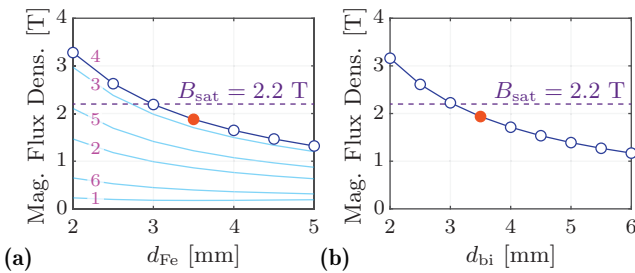


Fig. 13: Results of the third optimization step. (a) Average magnetic flux density for the six different locations in the stator core indicated in **Fig. 8 (a)** (above each slot) versus the thickness d_{Fe} . (b) Average magnetic flux density at the middle of the mover back iron versus the thickness d_{bi} .

V. HARDWARE PROTOTYPE

This section describes the hardware prototype of the selected LA design and the test bench needed to conduct its experimental verification, highlighting the practical realization choices made.

A. Stator Realization

1) *Stator Core:* In order to greatly simplify the stator manufacturing and assembling, the stator core is segmented along the axial direction into multiple identical rings like the one shown in **Fig. 14 (b)**. As it can be seen from the reported cross section in **Fig. 14 (a)**, the length of each segment corresponds to a stator pitch $\tau_s = 4$ mm, spanning exactly the width of one tooth and two half slots. This way, it is possible to machine the ring down to the desired tooth thickness of $l_{Fe} = 1.6$ mm and also realize the thin pole shoe solidly together with the tooth. Furthermore, this shape allows to insert and firmly hold in place a single coil between two stator rings. The material used is the desired *VACOFLUX50*, whose magnetization curve is measured experimentally on a toroidal sample [22] and reported in **Fig. 14 (c)**. From this, it is possible to estimate the worst-case core losses, i.e. assuming that all the material experiences the full variation of magnetic flux density with amplitude $\Delta B = 2$ T. The encircled area on the B - H plane, multiplied by the volume of the stator core and $f_{op} = 5$ Hz results in $P_{Fe} = 3.18$ W. Nevertheless, due to the machine geometry and operation, the FEM simulations show that no part of the stator core experiences such large swing in B , but rather $\Delta B \approx 1$ T with a $B_{DC} = 0.5$ T DC bias is a more realistic average approximation. For the sake of simplicity, the DC bias is hereby neglected, otherwise a displacement factor [22] needs to be considered. According to the dependence of P_{Fe} on B^β with $2 < \beta < 3$ in the Steinmetz equation, the core losses will be at least lower than $P_{Fe} = 0.8$ W.

2) *Coils:* The coils are custom-made as well (cf. **Fig. 14 (e)**), with the aim of maximizing the fill factor k_{ff} of the chosen copper cross section. Importantly, the selection of the number of turns N takes into account the specifications of the inverter driving the LA. This is compactly realized based on the IC *MP6535* by *Monolithic Power Supply*. The maximum current that this module can supply is $I_{inv,lim} = 5$ A and the maximum allowed DC-link voltage is $U_{DC,max} = 26$ V. A larger N reduces the inverter current \hat{I}_{inv} and is therefore beneficial as the conduction losses of the inverter's switches are also reduced. Nevertheless, the induced voltages $u_{q,\{a,b,c\}} = N u_{q,\{a,b,c\},1}$ increase to the point that it might not be possible to impress the necessary current during operation. In fact, by simple inspection of the equivalent circuit in **Fig. 14 (d)** and considering that the LA is realized with two coils in series per phase, the applied phase voltages need to be $u_{\{a,b,c\}} = 2 R_c i_{\{a,b,c\}} + 2 u_{q,\{a,b,c\}}$. Note that the voltage drop on the inductance L_c is neglected due to the low operating frequency $f_{op} = 5$ Hz. The inverter can only provide a maximum voltage $U_{\{a,b,c\},max} = U_{DC,max}/2 = 13$ V. In order to check that this limit is respected, the single-turn flux linkages $\psi_{\{a,b,c\},1}(t)$ of each coil are obtained from the FEM simulations and integrated, showing that a maximum

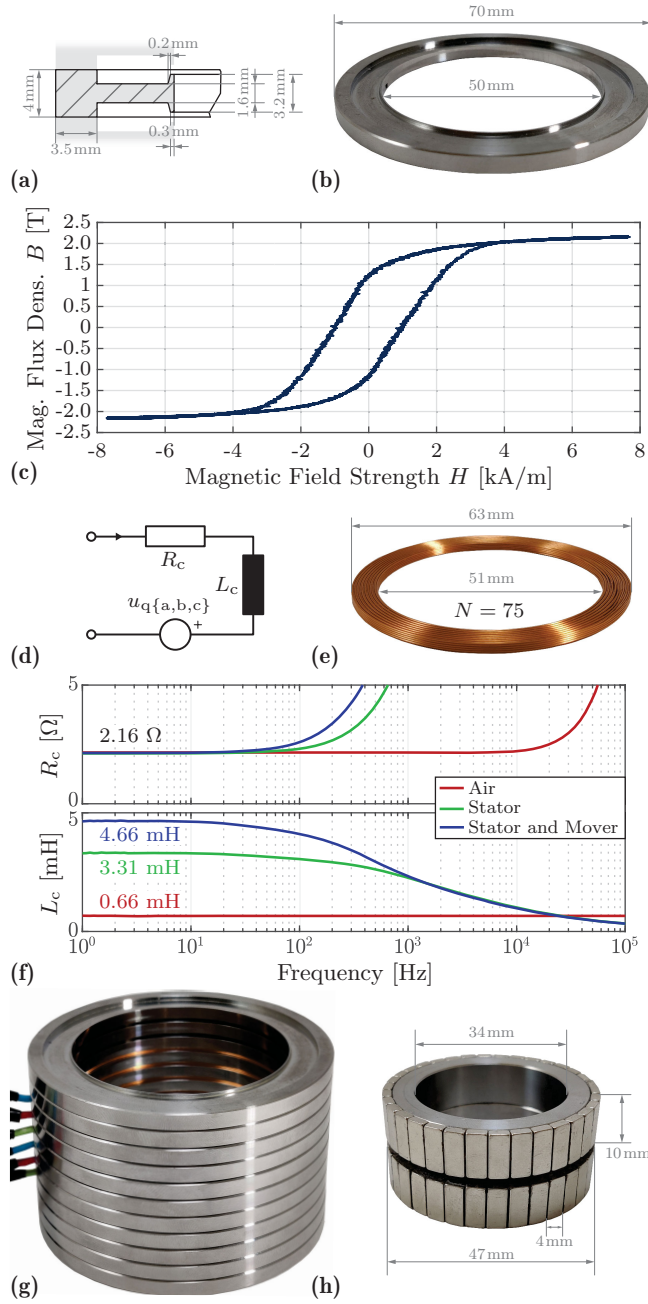


Fig. 14: Realized hardware prototype of the TLA. (a) Stator cross section with annotated dimensions. (b) Realized stator ring made of VACOFLUX50. (c) Magnetization curve of VACOFLUX50, measured on a toroidal material sample at $f_{op} = 5 \text{ Hz}$ with two windings. One is used to impress the sinusoidal magnetizing current and the other one to measure the induced voltage, which is then integrated and divided by the cross section of the sample. (d) Equivalent circuit of a stator coil, consisting of the resistance R_c , the inductance L_c and the induced voltage $u_{q\{a,b,c\}}$. (e) Realized stator coil made of a 0.40 G1B coated copper wire with $N = 75$ turns. (f) Measured electrical characteristics of the realized stator coils versus frequency, using an impedance analyzer (Omicron Lab Bode100). Three cases are compared: in air, in stator without and with mover. The curves show that high frequency effects (eddy, skin and proximity) appear. (g) Overall stator assembly with stacked segments equipped with coils. (h) Realized mover with two stacked back iron rings and segmented PMs. Each segment is $w_{PM} = 4 \text{ mm}$ wide and $l_{PM} = 10 \text{ mm}$ long.

voltage of $U_{q,1,\max} = 27 \text{ mV}$ is induced per turn. The number of turns that can be fitted by the manufacturer with a 0.40 G1B coated wire in the given cross section is $N = 75$. The resulting fill factor is $k_{ff} = 0.53$, the inverter current is $I_{inv,\max} = 2.2 \text{ A}$ and the maximum induced voltage is $U_{q,\max} = 4.05 \text{ V}$. This results in a maximum phase voltage $U_{\{a,b,c\},\max} = 11.9 \text{ V}$, which leaves some margin from the inverter limit. The electrical characteristics of the coil are measured and reported in **Fig. 14 (f)**. The DC coil resistance is $R_c = 2.16 \Omega$. The inductance is measured for three different conditions, i.e. in air and when mounted on the stator without and with mover inserted. The last case is the one to be considered to tune the current controller. The final stator assembly with the realized stator core rings and coils can be seen in **Fig. 14 (g)**.

B. Mover Realization

The mover consists of the back iron and the PMs. The former is also made of VACOFLUX50 and is built from two simple rings with the dimensions indicated in **Fig. 14 (h)**. The radially magnetized SPMs are not only quite fragile if realized as a single ring-shaped piece, but also extremely difficult/expensive to manufacture with the correct magnetization direction. For this reason, multiple small, axially magnetized, rectangular PMs are used. They are glued on the outer surface of the back iron, one adjacent to the other as shown in **Fig. 14 (h)**. Their thickness is the chosen $d_{PM} = 2 \text{ mm}$ and their width is $w_{PM} = 4 \text{ mm}$. The magnetization grade is N50. Such PMs are commercially available and rather inexpensive to purchase, and they well-approximate the desired magnetization profile. The correct polarity of each PM is verified during the gluing process with a magnetometer. The final weight of the mover is $m_{mov} = 148 \text{ g}$. The complete hardware prototype of the *ShuttlePump* is finally shown in **Fig. 15**.

C. Experimental Test Bench

In order to verify experimentally the functionality of the realized LA prototype, a custom multi-purpose test bench is built. There are two possible variants, shown in **Fig. 16**: one that can be used to measure axial forces and one that is specifically needed to measure the radial attraction force.

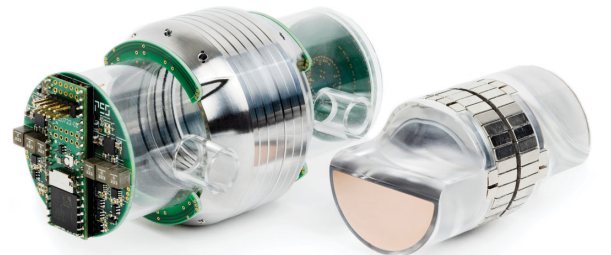


Fig. 15: Complete hardware prototype of the *ShuttlePump* with its drive system, consisting of the drive and control unit, linear-rotary position sensors [8] and the LiRA (stator and mover).

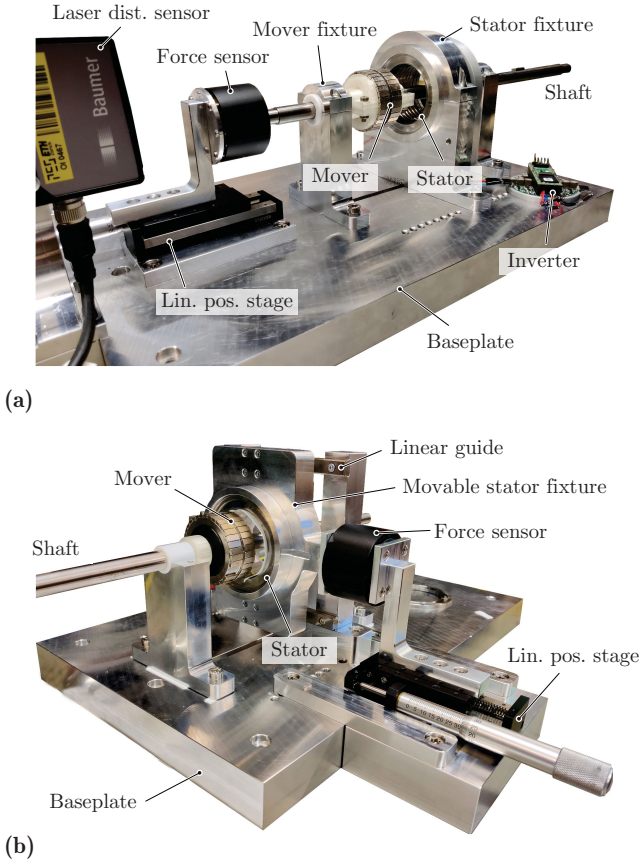


Fig. 16: Experimental test bench. (a) Variant for axial force measurements with fixed stator and movable mover along the axial direction. (b) Variant for radial attraction force measurements with fixed mover and movable stator along the radial (x - only) direction.

1) *Axial Force:* In order to measure the axial force, the TLA is mounted as in **Fig. 16 (a)**. The stator is firmly held in place with a clamp fixture directly mounted to the baseplate. The mover is mounted on a shaft and can only move along the axial direction. The shaft is supported on the two sides by teflon bearings for minimum friction. At the end of the shaft there is a linear positioning stage on which a force sensor (Rokubi, BOTA Systems) is mounted. To prevent the effect of unwanted backlashes coming from the linear positioning stage during measurements, the shaft and the force sensor are not connected together. Instead, the axial force is measured by energizing the TLA and pushing with the sensor against the shaft of the mover.

2) *Radial Attraction Force:* For this measurement, it is necessary to adjust the radial position of the mover, so it can be displaced away from the center of the machine. It is decided to fix the mover (also axially) and adjust the stator position instead. Therefore, the stator clamp is adapted as shown in **Fig. 16 (b)** and mounted on two linear guides, which constrain the radial movement horizontally (along the x -axis). This time, the linear positioning stage and the force sensor are placed on the side of the movable stator clamp.

VI. EXPERIMENTAL VERIFICATION

The experimental measurements conducted on the hardware prototype of the LA are reported in this section. The verification includes measurements of the radial attraction force and the profile of the drive force along the axial direction. From the latter, the machine constant k_m is obtained.

A. Radial Attraction Force Measurements

In order to measure the radial attraction force, the LA is mounted on the corresponding test bench (cf. **Fig. 16 (b)**). It is ensured that the axis of the mover is well-aligned with the axis of the stator, especially in the y -direction. The x -position is adjusted in steps of $10\mu\text{m}$ and for each position the output of the force sensor is recorded for 10 s and averaged. The measurements are reported in **Fig. 17** for positive displacements in the x -direction. This is because the linear positioning stage can sustain a high load force only in one direction. It can be observed that the measured values are in good agreement with the simulated ones. They are obtained from a full 3D FEM simulation with the non-linear material definition for VACOFLUX50. It can be seen that, for the maximum displacement $x_{\text{mov}} = 140\mu\text{m}$, the obtained radial attraction force is $F_{\text{rad}} = 23.8\text{N}$, which is in agreement with what is expected from the design space.

B. Machine Constant - Axial Force Profile

The measurements of the axial force profile are carried out using the test bench of **Fig. 16 (a)**. The mover is initially positioned at $z_{\text{mov}} = 10\text{mm}$, i.e. at one end of the LA. Then, a q -current with constant amplitude $\hat{I} = 1\text{A}$ is impressed and controlled in the winding. The phase currents $i_{\{a,b,c\}}$ fed by the inverter are determined from the electrical angle ϑ for MFPA, hence for each axial position of the mover z_{mov} , $\vartheta = \frac{2\pi}{l_{\text{act}}}z_{\text{mov}}$ is assigned. At this point, the mover is slowly pushed inside the LA with the help of the linear positioning stage, till it reaches $z_{\text{mov}} = -10\text{mm}$, i.e. the other end of the actuator. During the process, the force sensor is in contact with the shaft on which the mover is mounted and measures the axial force F_{ax} pushing against it. Simultaneously, the position

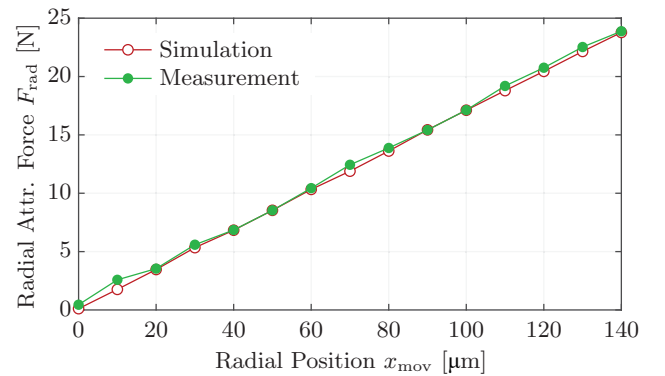


Fig. 17: Radial attraction force F_{rad} versus the mover's radial position x_{mov} . For comparison, the simulated forces from the corresponding 3D FEM model with realistic non-linear material definitions for VACOFLUX50 are reported.

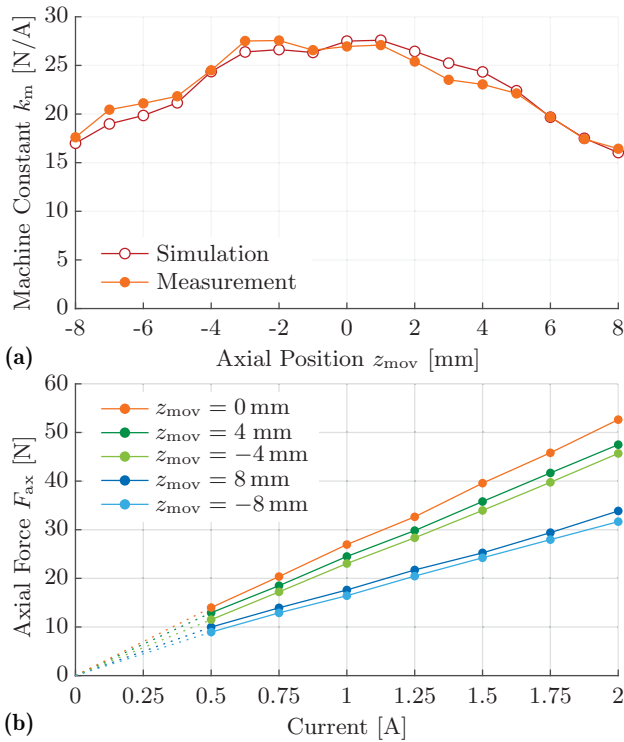


Fig. 18: (a) Axial force profile measured for $\hat{I} = 1$ A (corresponding to the machine constant k_m) compared to the values obtained by the non-linear 3D FEM simulation with $N\hat{I} = 75$ Aturns. (b) Linearity of the measured axial force versus the impressed current amplitude at different axial positions of the mover.

of the mover is measured with a laser distance sensor (*Baumer OM70-P0140*) and recorded. With this method, the points of **Fig. 18 (a)** are obtained. The values of the measured forces are equivalent to the machine constant k_m , as the impressed current amplitude is unitary. If the measured machine constant is compared to the results of the full non-linear 3D FEM simulations, it can be seen that they are in agreement, with an average absolute error of 3.2% over the whole profile, with slightly higher values for the negative z_{mov} -axis (peaking at 7.7% for $z_{mov} = -7$ mm). Also the reduction of k_m with $|z_{mov}|$ to 2/3 of its value at $z_{mov} = 0$ mm is verified. Moreover, the cogging force component is visible from the measurements and its amplitude can be estimated to be $\hat{F}_{cog} \approx 1$ N. Most importantly, with the measured k_m it is possible to calculate the instantaneous copper losses and their average over one period of operation with the same procedure discussed in **Sec. IV-A2** and **Fig. 9**. The result is a continuous copper power loss of $P_{Cu,avg} = 7.9$ W. Adding the estimated core losses $P_{Fe} = 0.8$ W and comparing to the required mechanical output power $P_{mech,avg,LA} = 3.6$ W, an efficiency of $\eta_{LA} = 41.4\%$ is obtained. Finally, another aspect to verify is the linearity of the generated axial force with respect to the current amplitude. **Fig. 18 (b)** shows the force measurements at different axial positions for increasing values of the current amplitude in steps of 0.25 A till $\hat{I} = 2$ A. This is the maximum value that the inverter can continuously sustain due to thermal limitations. For all measured cases, the maximum percent non-linearity does not exceed 2%.

VII. CONCLUSION

Implantable TAHs like the the *ShuttlePump* require highly-compact actuators and drive systems to enable their pumping operation. Their design is challenging and has to satisfy numerous stringent constraints and requirements imposed by the application. In this paper the analysis, design, realization and experimental verification of the LA of the *ShuttlePump* were presented. With the realized compact hardware prototype it is possible to meet the axial force requirements (up to 43 N peak) with 7.9 W of continuous power losses, which is below the specified limit of 10 W and hence prevents the risk of blood damage due to heating. Furthermore, the measured maximum radial attraction force of 23.8 N acting on the mover is within the specified allowed radial load of the hydrodynamic bearing supporting the piston during operation. Future work includes the design and realization of the RA part, which together with the linear-rotary position sensors [8] will enable full closed-loop linear-rotary position control. Based on this, it will be possible to verify the pumping operation of the *ShuttlePump* *in vitro*, i.e. on a dedicated hydraulic test bench.

REFERENCES

- [1] G. Savarese and L. H. Lund, "Global Public Health Burden of Heart Failure," *Cardiac Failure Review*, vol. 3, no. 1, pp. 7–11, 2017.
- [2] M. C. Alraies and P. Eckman, "Adult Heart Transplant: Indications and Outcomes," *Journal of Thoracic Disease*, vol. 6, no. 8, p. 1120, 2014.
- [3] J. L. Vieira, H. O. Ventura, and M. R. Mehra, "Mechanical Circulatory Support Devices in Advanced Heart Failure: 2020 and Beyond," *Progress in Cardiovascular Diseases*, vol. 63, no. 5, pp. 630–639, 2020.
- [4] R. A. Beauré, O. H. Frazier, and J. A. Morgan, "Total Artificial Heart Implantation as a Bridge to Transplantation: a Viable Model for the Future?" *Expert Review of Medical Devices*, vol. 15, no. 10, pp. 701–706, 2018.
- [5] K. G. Phillips, N. K. Ranganath, and N. Moazami, "Status and Availability of a Total Artificial Heart," in *Mechanical Support for Heart Failure*, pp. 191–206. Springer, 2020.
- [6] M. Granegger, T. Bierewitz, M. Nicolai, and U. Kertzscher, "Blood Pump," EU Patent WO/2022/049166, Mar 10, 2022.
- [7] T. Bierewitz, K. Narayanaswamy, R. Giuffrida, T. Rese, D. Bortis, D. Zimpfer, J. W. Kolar, U. Kertzscher, and M. Granegger, "A Novel Pumping Principle for a Total Artificial Heart," TechRxiv, Mar 27, 2023, doi: 10.36227/techrxiv.22309336.v1. [Online]. Available: https://www.techrxiv.org/articles/preprint/A_Novel_Pumping_Principle_for_a_Total_Artificial_Heart/22309336
- [8] R. V. Giuffrida, J. W. Kolar, and D. Bortis, "Eddy-Current Linear-Rotary Position Sensor for an Implantable Total Artificial Heart," in *Proc. of the 25th IEEE International Conference on Electrical Machines and Systems (ICEMS)*, pp. 1–6. IEEE, 2022.
- [9] N. K. Ranganath, M. Rashidi, J. F. Antaki, K. G. Phillips, Z. N. Kon, D. E. Smith, A. Reyentovich, and N. Moazami, "Mechanical Blood-Immersed Bearings in Continuous-Flow Rotary Blood Pumps," *ASAIO Journal*, vol. 66, no. 4, pp. 343–347, 2020.
- [10] E. Potapov, F. Kaufmann, A. Scandroglio, and M. Pieri, "Pump Thrombosis," in *Mechanical Circulatory Support in End-Stage Heart Failure*, pp. 495–512. Springer, 2017.
- [11] J. K. Kirklin, D. C. Naftel, R. L. Kormos, F. D. Pagani, S. L. Myers, L. W. Stevenson, M. A. Acker, D. L. Goldstein, S. C. Silvestry, C. A. Milano *et al.*, "Interagency Registry for Mechanically Assisted Circulatory Support (INTERMACS) Analysis of Pump Thrombosis in the HeartMate II Left Ventricular Assist Device," *The Journal of Heart and Lung Transplantation*, vol. 33, no. 1, pp. 12–22, 2014.
- [12] S. Mirić, R. Giuffrida, G. Rohner, D. Bortis, and J. W. Kolar, "Design and Experimental Analysis of a Selfbearing Double-Stator Linear-Rotary Actuator," in *Proc. of the IEEE International Electric Machines & Drives Conference (IEMDC)*, pp. 1–8. IEEE, 2021.
- [13] L. Xie, J. Si, Y. Hu, H. Feng, and K. Ni, "Characteristics Analysis of the Motions of the Two-degree-of-freedom Direct Drive Induction Motor," *IEEE Transactions on Industrial Electronics*, vol. 67, no. 2, pp. 931–941, 2019.

- [14] A. Z. Shukor and Y. Fujimoto, "Direct-drive Position Control of a Spiral Motor as a Monoarticular Actuator," *IEEE Transactions on Industrial Electronics*, vol. 61, no. 2, pp. 1063–1071, 2013.
- [15] P. Jin, H. Lin, S. Fang, and S. L. Ho, "Decoupling Control of Linear and Rotary Permanent Magnet Actuator Using Two-Directional dq-Transformation," *IEEE Transactions on Magnetics*, vol. 48, no. 10, pp. 2585–2591, 2012.
- [16] Z. Ling, J. Ji, J. Wang, and W. Zhao, "Design Optimization and Test of a Radially Magnetized Magnetic Screw with Discretized PMs," *IEEE Transactions on Industrial Electronics*, vol. 65, no. 9, pp. 7536–7547, 2017.
- [17] D. Timms, "A Review of Clinical Ventricular Assist Devices," *Medical Engineering & Physics*, vol. 33, no. 9, pp. 1041–1047, 2011.
- [18] N. Bianchi, S. Bolognani, D. Dalila Corte, and F. Tonel, "Tubular Linear Permanent Magnet Motors: An Overall Comparison," *IEEE Transactions on Industry Applications*, vol. 39, no. 2, pp. 466–475, 2003.
- [19] H. Hu, J. Zhao, X. Liu, Y. Guo, and J. Zhu, "No-load Magnetic Field and Cogging Force Calculation in Linear Permanent-Magnet Synchronous Machines with Semiclosed Slots," *IEEE Transactions on Industrial Electronics*, vol. 64, no. 7, pp. 5564–5575, 2016.
- [20] A. Souissi, I. Abdennadher, and A. Masmoudi, "An Approach to Reduce the Cogging Force in Tubular Linear PM Synchronous Machines," in *Proc. of the 10th International Conference on Ecological Vehicles and Renewable Energies (EVER)*, pp. 1–7, 2015.
- [21] T. M. Jahns and W. L. Soong, "Pulsating Torque Minimization Techniques for Permanent Magnet AC Motor Drives - A Review," *IEEE Transactions on Industrial Electronics*, vol. 43, no. 2, pp. 321–330, 1996.
- [22] G. Niedermeier and M. Esguerra, "Measurement of Power Losses with DC-Bias – The Displacement Factor," in *Proc. of the International Conference on Power Conversion/Intelligent Motion (PCIM)*, pp. 169–174, 05 2000.